ACS APPLIED MATERIALS & INTERFACES

www.acsami.org

Research Article

Remote Floating-Gate Field-Effect Transistor with 2-Dimensional Reduced Graphene Oxide Sensing Layer for Reliable Detection of SARS-CoV-2 Spike Proteins

Hyun-June Jang, Xiaoyu Sui, Wen Zhuang, Xiaodan Huang, Min Chen, Xiaolei Cai, Yale Wang, Byunghoon Ryu, Haihui Pu, Nicholas Ankenbruck, Kathleen Beavis, Jun Huang, and Junhong Chen*

Cite This: *ACS Appl. Mater. Interfaces* 2022, 14, 24187−24196

Read Online

ACCESS | Metrics & More | Article Recommendations | Supporting Information

ABSTRACT: Despite intensive research of nanomaterials-based field-effect transistors (FETs) as a rapid diagnostic tool, it remains to be seen for FET sensors to be used for clinical applications due to a lack of stability, reliability, reproducibility, and scalability for mass production. Herein, we propose a remote floating-gate (RFG) FET configuration to eliminate device-to-device variations of two-dimensional reduced graphene oxide (rGO) sensing surfaces and most of the instability at the solution interface. Also, critical mechanistic factors behind the electrochemical instability of rGO such as severe drift and hysteresis were identified through extensive studies on rGO−solution interfaces varied by rGO thickness, coverage, and reduction temperature. rGO surfaces in our RFGFET structure displayed a Nernstian response of 54 mV/pH (from pH 2 to 11) with a 90% yield (9 samples out of total 10), coefficient of variation (CV) < 3%, and a low drift rate of 2%, all of which were calculated from the absolute measurement values. As proof-of-concept, we demonstrated highly reliable, reproducible, and label-free detection of spike proteins of severe acute respiratory syndrome coronavirus 2 (SARS-CoV-2) in a saliva-relevant media with concentrations ranging from 500 fg/mL to 5 μg/mL, with an R^2 value of 0.984 and CV < 3%, and a guaranteed limit of detection at a few pg/mL. Taken together, this new platform may have an immense effect on positioning FET bioelectronics in a clinical setting for detecting SARS-CoV-2.

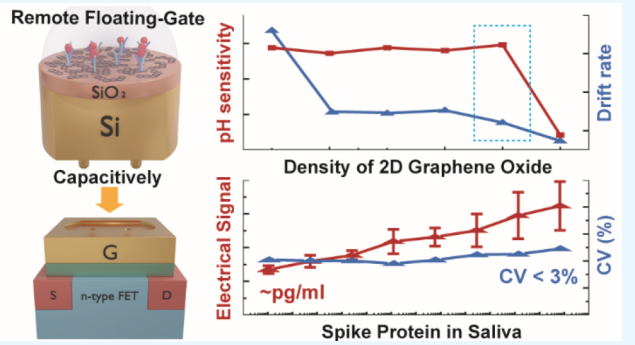

KEYWORDS: *SARS-CoV-2 biosensor, graphene oxides, RFGFET, drift, pH detection*

INTRODUCTION

The outbreak of coronavirus 2019 (COVID-19),[1] resulting from severe acute respiratory syndrome coronavirus 2 (SARS-CoV-2), has evolved into a global pandemic, causing more than 500 million infections and more than six million deaths (https://covid19.who.int/). The development of a reliable mechanism to track infectious diseases and their spread remains a challenge. Indeed, the early identification and diagnosis of potential pathogens is essential for preventing virus transmission.[2] The real-time reverse transcriptase polymerase chain reaction (RT-PCR) technique has been the gold standard for COVID-19 detection, but it can take hours to days to receive test results, as RT-PCR requires a large laboratory space, multistep sample preparation, and trained experts to perform the tests.[3] In contrast, several point-of-care (POC) testing tools based on lateral flow immunoassays (LFAs)[4] have been authorized by the U.S. Food and Drug Administration (FDA) for emergency use, which are still inadequate to precisely identify a particular phase of COVID-19 disease progression in patients.

Meanwhile, proof-of-concept field-effect transistors (FETs) have been demonstrated for COVID-19 detection using nanostructured materials such as carbon nanotubes,[5] graphene,[6] reduced graphene oxide (rGO),[7] and transition metal dichalcogenide monolayers.[8] Those FET sensors eliminate the multiple laboratory steps that are typically required to amplify DNA sequence or immobilize the specialized reagents or enzymatic labels, as demanded by LFAs, conventional fluorescence, luminescence, and radioactive assays. A few reports on two-dimensional (2D) FETs have already shown excessively low limit of detection (LOD) for SARS-CoV-2 spike proteins (S proteins) down to 1 fg/mL,[6] while the LOD observed from the conventional LFAs is measured as 5 ug/mL

Received: March 21, 2022
Accepted: May 7, 2022
Published: May 20, 2022

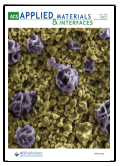

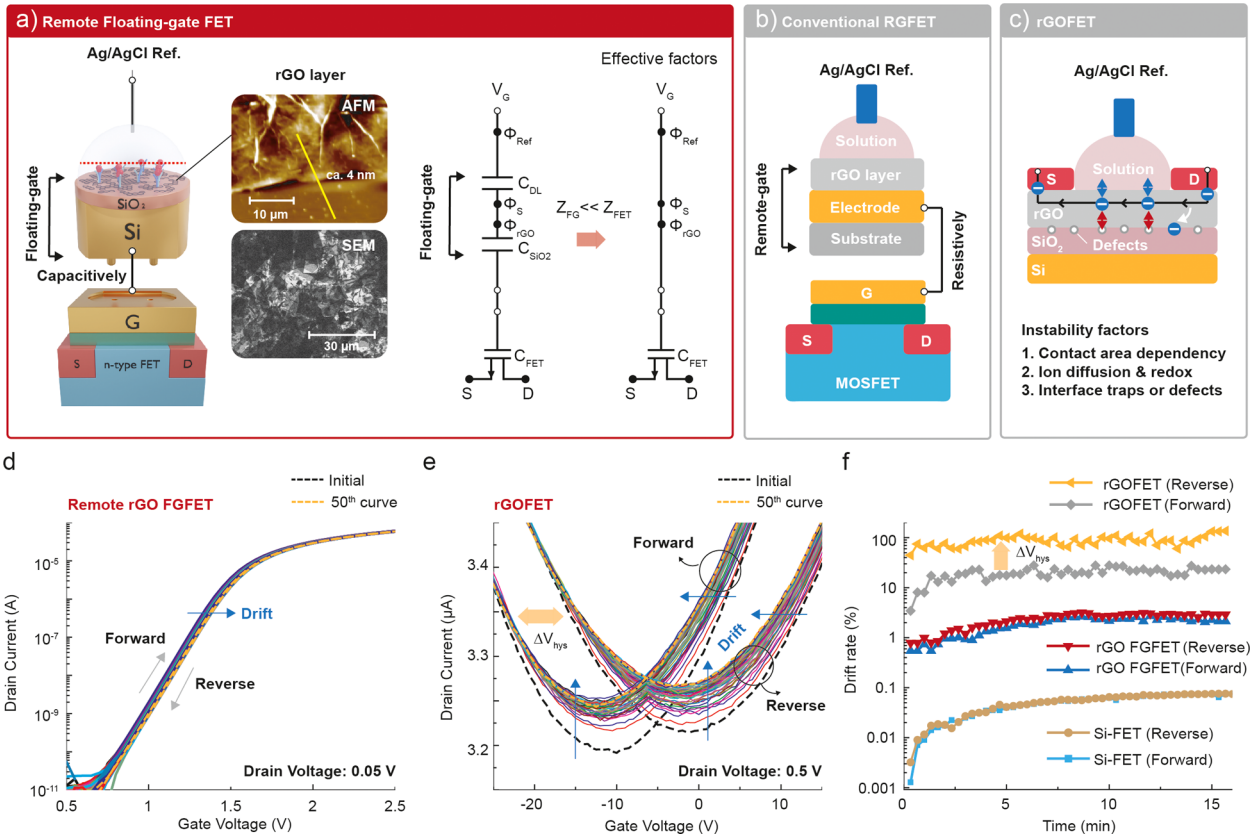

Figure 1. (a) Schematic images and equivalent circuits of the RFGFET system. AFM and SEM images of the 2D rGO layer on the FG surface made by a heat-assisted drop-casting method and reduced at 200 °C. Schematic images of (b) conventional RGFET and (c) rGOFET structure. (d) Transfer curves of rGO RFGFET measured for 50 gate voltage cycles in pH7 solution. (e) Transfer characteristics of rGOFET with rGO identically processed to (a) measured for 50 gate voltage cycles via the bottom gate without any solution environment on the rGO layer. (f) Drift rate of Si-FET, rGO RFGFET, and rGOFET.

in literature,[9] and capacities to screen SARS-CoV-2 in patient specimens.[6,7] However, to the best of our knowledge, none of FET sensors above has been authorized by FDA for emergency use or commercialized for clinical uses so far while most of impressive work has been shown for a single device scale accompanied by well-controlled laboratory environments for measurements.

A major technical hurdle of low-dimensional FET sensors[10−15] for POC market products is the lack of adequate control over the manufacturing quality for low-dimensional semiconducting layers.[16] As a result, electrical properties of low-dimensional materials easily fluctuate due to various factors such as grain boundaries, impurities, and defects, all of which if not adequately controlled over the fabrication process, could lead to random and inconsistent performance for the transducers.[17−20] Additional variation and instability could be introduced by directly placing a solution-gated system[21] on low-dimensional semiconducting layers as the gate; that is, the nanomaterial plays a role of both sensing membrane and transducer. Inevitable interactions between the semiconducting layer and the media solution in terms of drain or gate current flow cause degradation of the intrinsic electronic properties of nanomaterials through redox reactions and ion diffusion.[6,22] Furthermore, human saliva testing adds extra random factors in the measurement system such as different ionic concentrations, pH values, and amounts of mucus, while blood cells, epithelial cells, and enzymes which could easily cause false or nonspecific signaling of FET sensors. Thus, fundamental studies regarding device yield, stability, reliability, and reproducibility of low-dimensional materials are required for success of FET sensors toward rapid POC market products along with studies to achieve higher sensing performance.

It is well-known that SARS-CoV-2 gains entry into target cells via an initial binding interaction between the S protein and the angiotensin-converting enzyme 2 (ACE2) receptor on the host cell surface, followed by viral fusion and entry.[23] The S protein consists of a signal peptide, S1 subunit, S2 subunit, and transmembrane domain anchored in the viral membrane and expressed as a trimer. In the normal metastable, prefusion conformation of the S protein, the receptor-binding domain (RBD) of the S1 subunit is partially blocked, which prevents host cell entry. However, upon interaction with the host cell, proteases cleave the S protein into the S1 and S2 subunits, resulting in an open conformation that exposes the RBD and enables binding to ACE2. As the primary means for viral infection, the S protein is an ideal target for detecting SARS-CoV-2 in patients.

In this paper, we propose a new remote floating-gate (RFG) FET configuration (Figure 1a) with two-dimensional (2D) reduced graphene oxide (rGO) that eliminates nonreliable behaviors of solution interfacial properties for reliable and reproducible COVID-19 sensing applications. The rGO layer is electrically isolated by an insulator, while confining a 2D structure of the rGO layer only to the solution interface, and capacitively connected to the gate of FET transducer. The

https://doi.org/10.1021/acsami.2c04969
ACS Appl. Mater. Interfaces 2022, 14, 24187−24196

proposed structure blocks any current flows into rGO which avoids any undesirable effects from interface traps, defects, and redox reactions. As a result, highly uniform absolute levels of threshold voltage (V_{th}), that is, intrinsic interfacial potentials of the rGO layer, are obtained for specific pH levels by the RFGFET. In addition, the rGO sensing membrane is highly sensitive to interfacial potential changes that are caused by protein binding on rGO layers due to the 2D structure of rGO isolated into solution interface with a high surface-to-volume ratio.

Using RFGFET platform, we first discovered critical mechanistic factors of rGO sensing layers behind drift and hysteresis in pH testing studies that were varied by device structure, rGO thickness, rGO coverage, and rGO reduction temperature. Our optimized rGO layer presented a Nernstian sensitivity of 54 mV/pH with an R^2 of 0.998 and a coefficient of variation (CV) < 3%, a 90% yield (9 samples out of total 10), a low drift rate of 2%, and no hysteresis, all of which are directly calculated from a directly measured V_{th} of rGO for each pH. Also, this optimized rGO layer led to a reproducible sensitivity of SARS-CoV-2 S proteins (6.3 mV/dec) in the PBS buffer solution with a concentration range from 3.4 pg/mL to 34 ng/mL with an R^2 value of 0.986. Also, the sensitivity of S protein in a saliva-relevant media was measured to be 5.1 mV/dec in a range from 500 fg/mL to 5 μg/mL, with an R^2 value of 0.984 and CV < 3%, while the guaranteed LOD is at a few pg/mL. Taken together, this work provides a novel platform for POC testing of COVID-19 that is rapid, sensitive, selective, reproducible, and reliable.

RESULTS AND DISCUSSION

Structural Advantages of RFGFET. Four nm-thickness multilayer rGO on a 300 nm-thick SiO_2 is capacitively coupled to the commercial FET transducer (Figure 1a). The 2D structure offered by the rGO layer is only confined to the solution interface on the FG by the SiO_2 insulator, which preserves the high surface-to-volume ratio for the sensing section. In contrast, it is challenging to avoid any influences of the bulk electrode underneath rGO layers for resistive connections of rGO layer[24,25] utilized in the conventional RGFET (Figure 1b) since the rGO layer is electrically coupled to the bulk electrode. That is, rGO and electrode complexes are regarded as a single combined resistor under the solution contact for a conventional RGFET, losing structural advantages offered by rGO layers at the solution interfaces. In addition, these rGO layers typically have imperfect coverage of rGO nanosheets on the electrode as shown in a scanning electron microscopy (SEM) image (Figure 1a), suggesting the inevitability of the uncovered electrode on interfacial potentials of the conventional RGFET system (Figure 1b) as being directly exposed to the solution.

An input impedance of commercial FET chip is at least 100 times higher than those of remote FG structure (Supporting Information (SI) Figure S1). Consequently, V_{th} of the RFGFET is an independent variable from factors that could alter the impedance of remote FG modules such as the thickness of the FG materials and SiO_2 and the contact area of media on the FG surface. Thus, an equivalent circuit simplified with effective factors for RFGFET (Figure 1a) is identical to that of RGFET.[26]

Importantly, rGO RFGFET strongly resists drift and hysteresis in transfer curves measured for 50 gate voltage cycles in a pH7 media solution (Figure 1d). A high gate input impedance of the commercial FET and the SiO_2 dielectric of the FG module prevents the electric current flow into the rGO, which leads to a large enhancement of stability by avoiding any undesirable factors impacting the rGO layers such as defects, interface traps, diffused ions, and redox reactions.

On the other hand, rGO layers processed identically to those in rGO RFGFET but used as a semiconducting channel for rGOFET (Figure 1c) reveal huge drifts and hysteresis in Dirac points (Figure 1e); for rGOFET biosensors, the rGO layer serves as both a semiconducting channel and a sensing layer. Such severe device instability in Figure 1e was observed without any solution environments applied on rGO layers; in solutions there are several extra contributing factors such as mobility of rGO layers, defects, interface traps, diffused ions from solution to the rGO layer, redox reactions, and area of solution contact on the rGO layer. As a result, our RFGFET structure achieved a 50-fold decrease in the drift rate at the maximum compared to that of rGOFET (Figure 1f). The drift rate was calculated at a difference in the V_{th} levels of RGFET and Si-FET between the initial and saturated states divided by V_{th} at the initial; Dirac points of rGOFET were used for the calculation.

The V_{th} of RFGFET is comprised of the sum of independent components such as the V_{th} of a commercial FET (V_{FET}) and the electrochemical potentials associated with a solution/RG system.[27]

$$V_{th} = V_{FET} + E_{ref} + \phi_{lj} - \varphi_s + \chi_{sol} + \frac{\phi_{RG}}{q} \quad (1)$$

where E_{ref} is an absolute potential of the Ag/AgCl reference electrode (0.316 V, GAMRY Instruments), ϕ_{lj} is the liquid junction potential difference, φ_s is the surface potential at the electrolyte/sensing film interface, χ_{sol} is the electrolyte-insulator surface dipole potential, and ϕ_{RG} is the work function of the RG material. V_{FET} and the transconductance (G_m) of an innate FET (G_{FET}) remains stable at 1.55 V and 63 μS, respectively, over time without any drift and hysteresis before introducing a new variable of solution interface (SI Figure S2). Therefore, we further define a standard electrochemical potential of the remote FG material (E_{RG}) using eq 1.

$$E_{RG} = \phi_{lj} - \varphi_s + \chi_{sol} + \frac{\phi_{RG}}{q} \quad (2)$$

E_{RG} is a value only associated with the intrinsic electrochemical potentials of the FG surface, the media solution, and their interfaces resulting from their contacts, independent of the V_{FET} and E_{ref} which are varied by different experimental setups. Here, each E_{RG} and G_m of the RFGFET measured by a forward and reverse sweeping mode is referred to as E_{RG}^{For}, E_{RG}^{Rev}, G_m^{For}, and G_m^{Rev}, respectively. The hysteresis in E_{RG} (ΔE_{hys}) and in G_m (ΔG_{hys}) herein are calculated as the difference in E_{RG} and G_m between forward and reverse sweeping mode at the saturation regime, respectively. G_m loss is calculated as $(G_{FET}-G_m)/G_{FET}$; a larger G_m loss will be shown at unstable solution interfaces and nonconductive surfaces.[28,29]

Mechanistic Factors of rGO Layers. Various thicknesses and coverages of rGO layers were prepared on a (3-aminopropyl)trimethoxysilane (APTMS)-treated SiO_2 surfaces by either controlling the concentrations of spin-coating GO solutions (SI Figure S3a) or using heat-assisted drop-casting methods (SI Figure S3b). Increasing the concentrations of spin-coating GO solutions (0.12, 0.24, 0.48 to 0.59 mg/mL)

https://doi.org/10.1021/acsami.2c04969
ACS Appl. Mater. Interfaces 2022, 14, 24187−24196

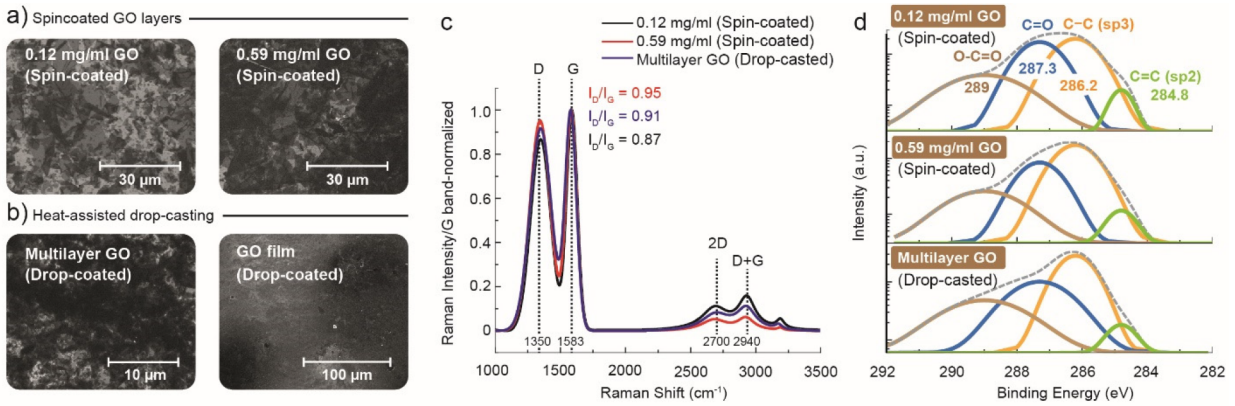

Figure 2. SEM images of rGO layers (a) spin-coated with 0.12 and 0.59 mg/mL GO solutions and (b) made by a heat-assisted drop-casting method. (c) Raman and (d) XPS spectra of rGO layers spin-coated with 0.12 and 0.59 mg/mL GO solutions, and multilayer rGO made by a heat-assistant drop-casting method, respectively. All rGO layers were reduced at 200 °C.

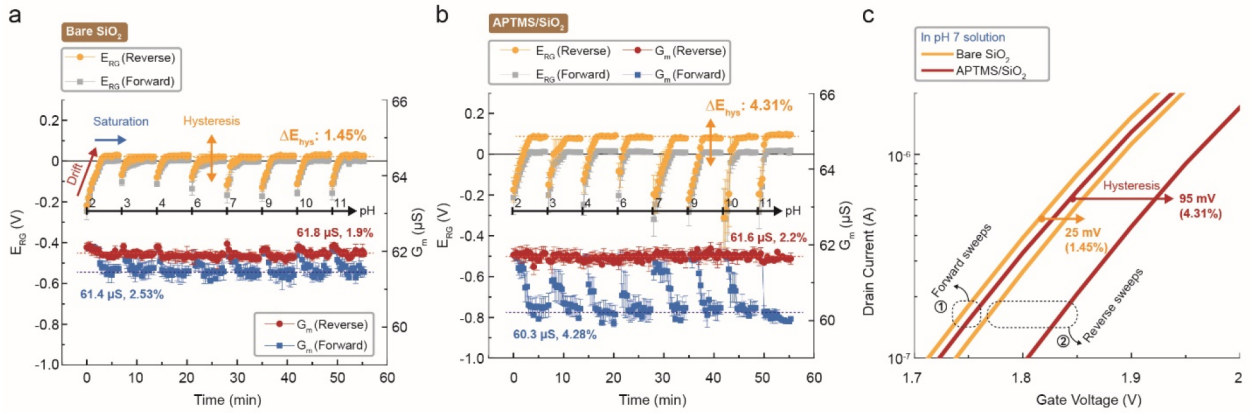

Figure 3. E_{RG} and G_m distributions of (a) SiO_2 and (b) APTMS that are measured by forward- and reverse-sweeping modes with increasing pH values over time. Each E_{RG} and G_m is averaged with at least seven trials for each measurement. (c) Representative transfer curves of SiO_2 and APTMS at saturation regime in pH7.

achieved denser rGO networks, but still showed discontinuity over the remote FG surfaces (Figure 2a, SI Figure S3a). In contrast, we obtained essentially continuous multilayer rGO (Figure 2b, SI Figure S3b) with ca. 4 nm-thickness (measured by atomic force microscopy (AFM) image in Figure 1a) using heat-assisted drop-casting methods with the high evaporation rate of GO solution under 120 °C (SI Figure S4). Additionally, ca. 2.5-μm-thick rGO films were made on the edge of wafer for this heat-assisted drop-casting condition (SI Figure S4). It is noted that the lower plate temperature at 50 °C led to thick rGO depositions over most of the wafer area (SI Figure S4c) instead of achieving multilayer rGO.

Similar Raman spectra were observed for rGO layers made by different depositions of spin-coating and heat-assisted drop-casting, showing the D band at 1350 cm^{-1}, which is attributed to the structural disorder, and the G band at 1583 cm^{-1}, which is attributed to the bond stretching of sp^2 carbon atoms (Figure 2c). The appearance of weak and broad 2D (2700 cm^{-1}) and D + G (2940 cm^{-1}) bands in the GO spectrum is also a signature of edge disorder in graphitic sheets due to the incorporation of oxygen functional groups. Similar I_D/I_G ratios of 0.87, 0.95, and 0.91 were obtained for all rGO layers, which were spin-coated with 0.12 and 0.59 mg/mL GO solutions and made by heat-assisted drop-casting, respectively. Plenty of oxygen functional groups in all rGO layers were also found in an X-ray photoelectron spectroscopy (XPS) spectrum (Figure 2d), contributing to the pH-sensing capability of the rGO layers, as described in the next section.

pH Sensitivity without GO Layers on SiO_2 FG. The pH sensitivity of our starting materials such as a bare SiO_2 (Figure 3a, SI Figure S5) and an APTMS-treated SiO_2 (Figure 3b, SI Figure S6) was evaluated before introducing a GO layer. Initial negatively charged E_{RG}^{For} of both SiO_2 and APTMS FG surface (gray-colored data in Figure 3a,b) drifted up to about 0 V of E_{RG}^{For}. No pH sensitivity was obtained for both surfaces (SI Figure S7a). Transfer curves measured in pH 7 at the saturation regime (Figure 3c), while remaining in mostly identical transfer curves during the forward-sweeping mode, show that the hydrophobicity of APTMS (SI Figure S7b)[22] promoted a slow response of water dipole orientations at the reverse sweeps and resultant large increase of E_{RG}^{Rev}.[29] The ΔE_{hys} of SiO_2 and APTMS were measured to be 1.45 and 4.31%, respectively. This result corresponds to a higher G_m^{For} loss for APTMS (4.28%, Figure 3b) compared with that of the SiO_2 surface (2.53%, Figure 3a).

pH Sensitivity with GO Layers on FG. Pristine GO layers that were spin-coated by 0.12 mg/mL (Figure 4a, SI Figure S8) and 0.59 mg/mL (Figure 4b, SI Figure S9) GO solutions on APTMS have no pH responses without reduction. All E_{RG}^{For} (Figure 4a,b) was saturated near 0 V regardless of pH

https://doi.org/10.1021/acsami.2c04969
ACS Appl. Mater. Interfaces 2022, 14, 24187−24196

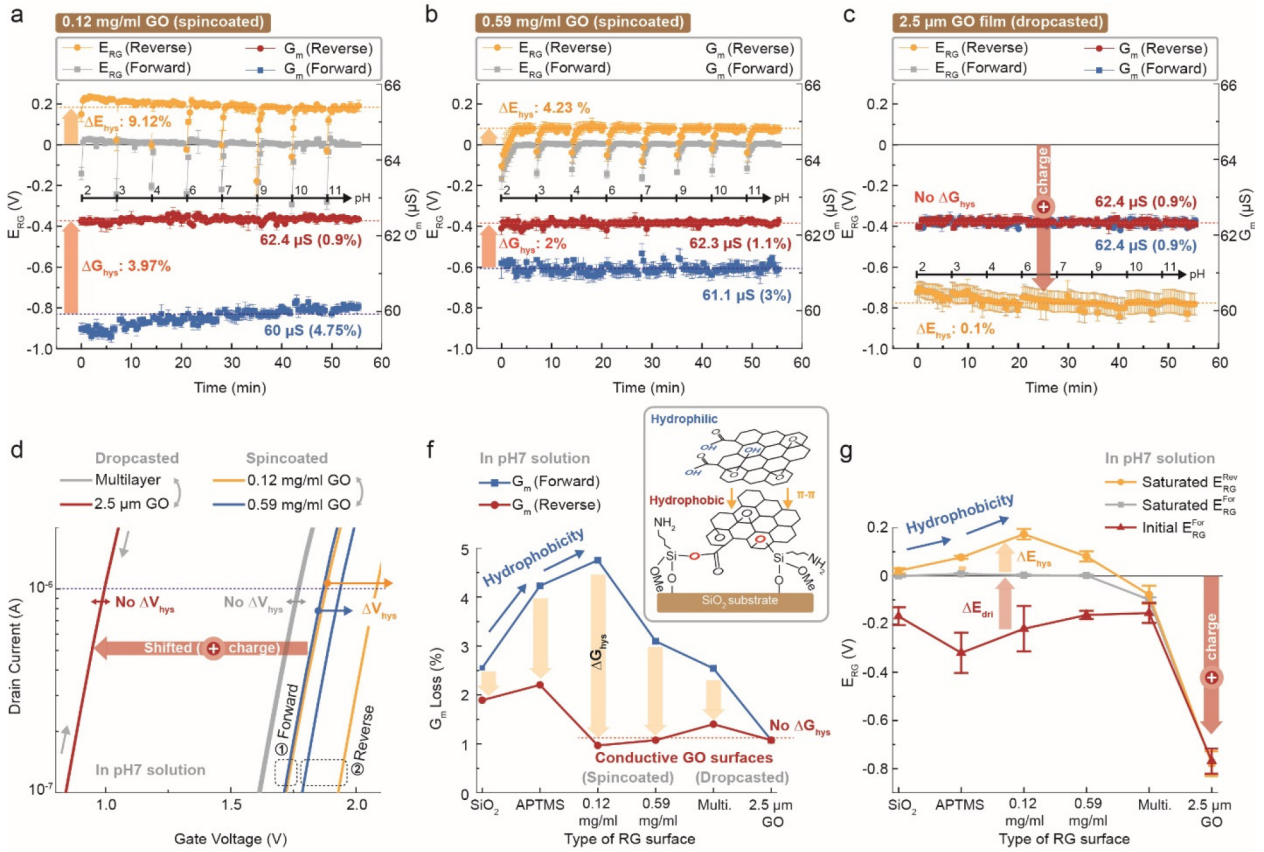

Figure 4. E_{RG} and G_m distributions over at least four samples with pristine GO surfaces spin-coated with (a) 0.12 mg/mL and (b) 0.59 mg/mL GO solutions and (c) 2.5 μm-thick GO films for increasing pH over time. (d) Representative transfer curves of spin-coated and drop-casted GO layers in pH7 at saturation regime. (e) E^{For}_{RG} distributions of spin-coated and drop-casted GO layers vs pH value. (f) G_m loss in pH7 vs the type of RG surface. Inset shows schematics for surface property changes by concentrations of GO flakes. (g) E_{RG} distributions in pH 7 at saturation regime vs the type of RG surface.

values, as were the cases of SiO_2 and APTMS. However, the presence of conductive GO layers under each condition was supported by higher G^{Rev}_m levels shown from spin-coated GO layers (0.12 mg/mL GO: 62.4 μS, 0.59 mg/mL GO: 62.3 μS) than APTMS (61.6 μS). On the other hand, 2.5 μm-thick GO films reveal insignificant ΔE_{dri}, ΔE_{hys}, ΔG_{hys}, and G_m loss, even though there is still no pH sensitivity (Figure 4c, SI Figure S10). Lower levels of E^{For}_{RG} and E^{Rev}_{RG} of ca. −0.8 V describe highly positive-charged GO surfaces while there are only 0.9% G_m loss with no ΔG_{hys}. There is a clear propensity that G^{For}_m increases with a higher conductivity of solution interface achieved by denser GO networks (SI Figure S11).

In summary, denser GO networks at the solution interface induce higher positive surface potentials with lower levels of E^{For}_{RG} and E^{Rev}_{RG} and ΔE_{hys}, as shown in a clear trend of transfer curves for each case measured for the pH7 buffer solution (Figure 4d). This reveals that highly conductive and hydrophilic GO films resist drift and hysteresis components. A very low concentration of GO networks at the solution-interface, such as 0.12 mg/mL GO has higher ΔE_{hys} (192 mV) and G^{For}_m loss (4.75%) than those of bare APTMS surfaces (ΔE_{hys}: 95 mV, G^{For}_m loss: 4.28%) as shown in Figure 4f,g. For this type of analytical tools for interfacial analysis, higher G^{For}_m loss and ΔE_{hys} are mostly shown for the solution interface with increased hydrophobicity.[29] Based on our observation, we could hypothesize that hydrophobicity of solution interfaces with a very low concentration of GO flakes on APTMS increased compared to that of a bare APTMS. It could be depicted that for lower GO concentrations most of the oxygen functional groups of monolayer GO on the surface are consumed in bonding with the amine groups on APTMS, which increases hydrophobicity. Furthermore, with increasing concentrations of GO, GO nanosheets begin to overlay on monolayer GO that had already bound to the surface via $\pi-\pi$ interactions, which exposes oxygen functional groups to the solution-interface steadily and increases hydrophilicity (inset of Figure 4f), suggesting some threshold in the concentration of GO flakes at the solution-interface to achieve hydrophilic surfaces.

pH Sensitivity with Reduction of GO. We further investigated the effects of reduction temperatures on the pH sensitivity of GO sensing layers (Figure 5). The pH responses of E^{For}_{RG} are shown for both 0.59 mg/mL GO (Figure 5a, SI Figures S12−S14) and 2.5 μm-thick GO films (Figure 5b, SI Figures S15−S17) reduced at 200, 300, and 400 °C, respectively. Overall E^{For}_{RG} levels of 0.59 mg/mL rGO steadily decreased at higher reduction temperatures (Figure 5a) due to the creation of positive charge carriers resulting from the reduction of diverse oxidized functional groups in GO sheets. Accordingly, increased conductivity resulting from higher reduction temperatures is shown as insignificant G_m loss (Figure 5c, SI Figure S18), suggesting a trade-off between the conductivity and pH sensitivity of rGO. This is also supported by the decreasing propensity in the pH sensitivity of rGO

https://doi.org/10.1021/acsami.2c04969
ACS Appl. Mater. Interfaces 2022, 14, 24187−24196

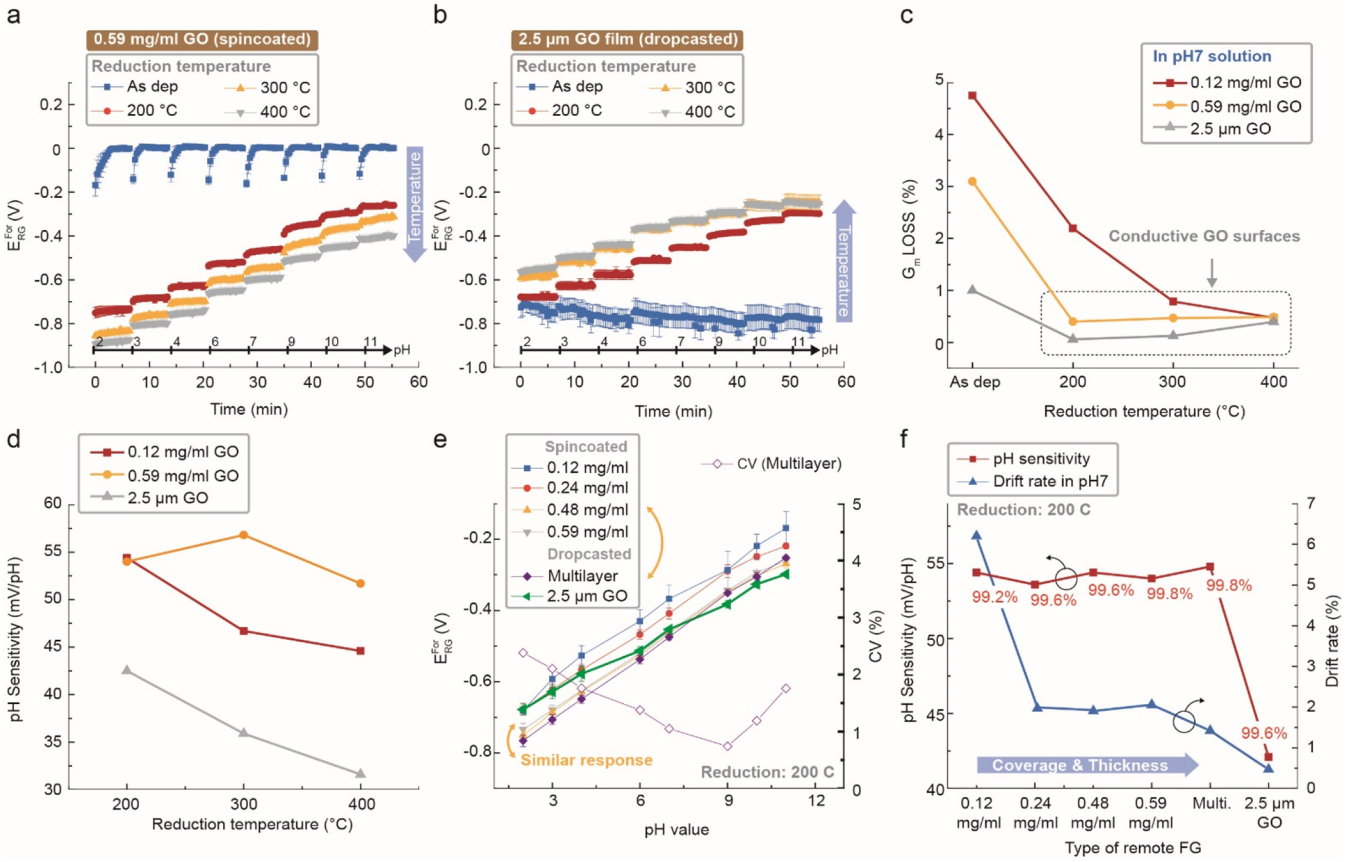

Figure 5. E_{RG}^{For} distributions of (a) 0.59 mg/mL rGO layers and (b) 2.5 μm-thick rGO films at different reduction temperatures over at least four samples as a function of increasing pH over time. (c) pH sensitivity of 0.12 and 0.59 mg/mL rGO layers and 2.5 μm-thick rGO film as a function of reduction temperature. pH sensitivity is directly calculated by using E_{RG}^{For} values. (d) G_m reduction of 0.12 and 0.59 mg/mL rGO layers and 2.5 μm-thick rGO film in pH7 vs the reduction temperature. (e) E_{RG}^{For} distributions of spin-coated or drop-casted rGO layers over at least four samples as a function of increasing pH; CV values of multilayer rGO were calculated by using V_{th} of nine different multilayer rGO layers for each pH showing a 90% yield (9 samples out of total 10). (f) pH sensitivity and drift rates in pH7 solutions.

layers with increasing reduction temperatures (Figure 5d, SI Figure S19). In contrast, 2.5 μm-thick rGO films increased E_{RG}^{For} levels overall with increasing reduction temperatures (Figure 5b), which is an opposite trend to that of 0.59 mg/mL GO. Without reductions, 2.5 μm-thick GO films already have plenty of positive charges because of the denser GO networks as shown in the lower E_{RG}^{For} levels at ca. −0.8 V (Figure 4c). Thus, the E_{RG}^{For} levels for 2.5 μm-thick rGO films are more affected by the losing effects of pH sensitivity from reductions.

Our results so far suggest that hydrophilic rGO surfaces that include oxygen functional groups are more sensitive to changes in surface potentials, and that the high conductivity of rGO surfaces stabilizes solution interfaces, thereby reducing hysteresis and drift components. Unfortunately, the higher conductivity achieved by higher reduction temperatures increases the hydrophobicity of the rGO surface. Thus, we sought to find the optimal pH sensitivity of rGO by increasing conductivity in terms of denser rGO networks under a minimized reduction temperature at 200 °C. Similar pH sensing properties were observed as rGO began to construct rGO networks that are dense enough over FG surfaces (i.e., 0.48 mg/mL rGO, 0.59 mg/mL rGO, multilayer rGO made by drop-casting, Figure 5e,f). CV values for each pH from multilayer rGO are <3% over all pH ranges; each CV value was calculated by using raw values of V_{th} for each pH over nine samples of rGO. Finally, the multilayer rGO made by the heat-assisted drop-casting method shows the lowest drift rate of 2%, thereby maintaining a high pH sensitivity of 54 mV/pH with an R^2 value of 0.998 (Figure 5f). More importantly, the optimal rGO layer revealed a 90% yield (9 samples out of total 10) in showing the pH sensitivity (54 mV/pH) due to enhanced stability and reproducibility of electrochemical properties of the RFGFET structure.

Spike Protein Detection Using rGO RFGFET. Quantification of S protein concentrations is done by using optimized multilayer rGO layers above. We tracked a shifting propensity of transfer curves of rGO RFGFET depending on the surface modification for S protein detection (Figure 6a). Summarized V_{th} and G_m loss for each interfacial condition is shown in Figure 6b. The V_{th} of bare SiO_2 and APTMS surfaces are close to 1.86 V in 0.05× PBS. On the other hand, the presence of multilayer rGO on an APTMS surface strongly induces positive charges on the FG surface, decreasing V_{th} to 1.35 V. The increase in G_m^{For} (APTMS: 60.3 μS → rGO: 62.7 μS) also suggests the formation of highly conductive rGO layers at the solution-FG interface.

In Figure 6b, neutralizing antibodies (n-antibodies) and bovine serum albumin (BSA) blocking layer, however, increase V_{th} relative to bare rGO surfaces (V_{th} of n-antibody/BSA: 1.43 V). It is noted that insignificant device-to-device variations are shown for all V_{th} levels with n-antibody probes on the rGO, which were obtained by averaging the absolute values of each

https://doi.org/10.1021/acsami.2c04969
ACS Appl. Mater. Interfaces 2022, 14, 24187−24196

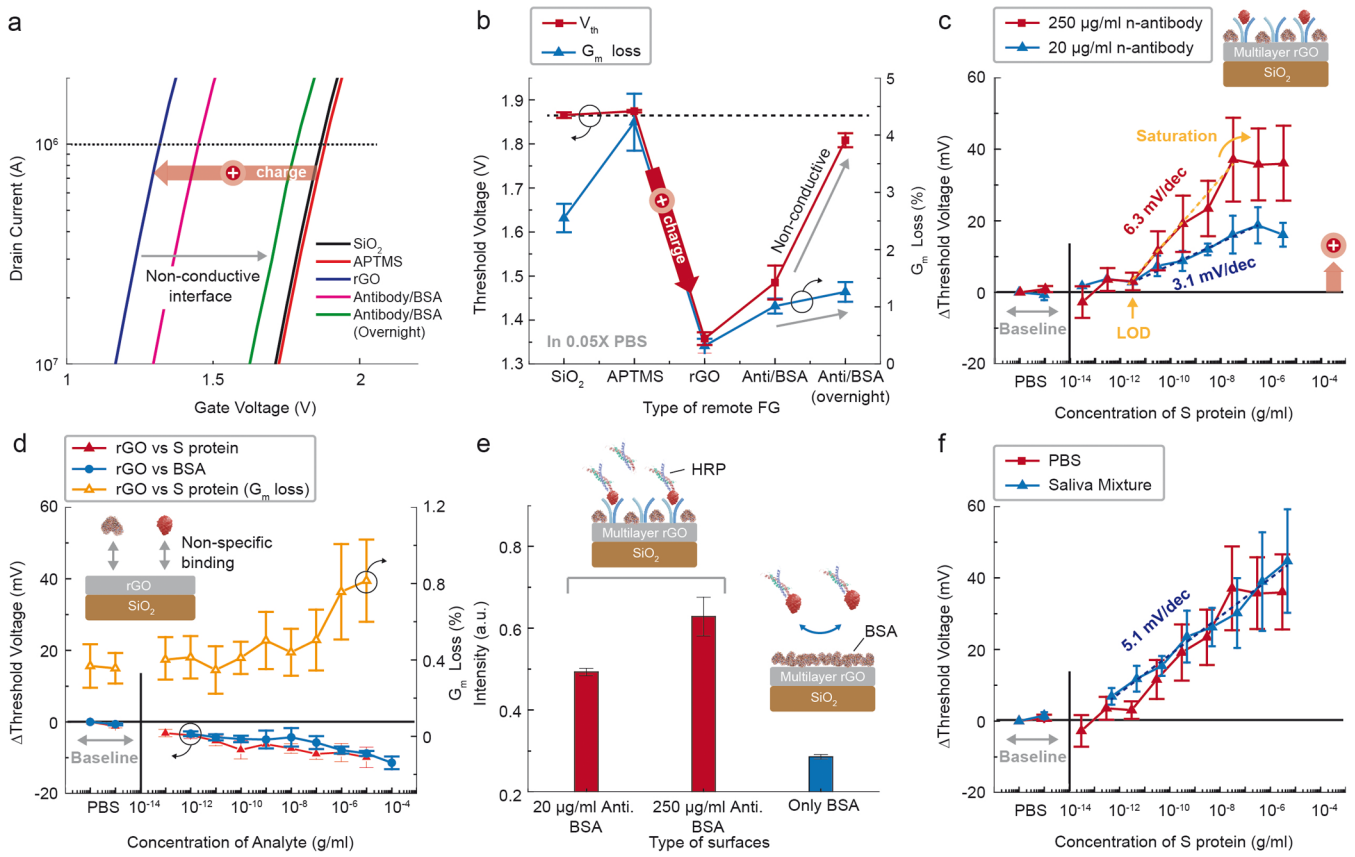

Figure 6. (a) Response of transfer curves depending on surface modifications on FG. (b) V_{th} and G_m^{For} distributions depending on surface modification on FG. (c) ΔV_{th} of n-antibody-functionalized rGO (20 or 250 μg/mL n-antibodies) vs concentrations of S protein. (d) ΔV_{th} or G_m^{For} loss of bare rGO vs concentrations of S protein or BSA. (e) ELISA detection of S protein using a n-antibody-conjugated rGO surface. (f) ΔV_{th} and CV of n-antibody-functionalized rGO (250 μg/mL n-antibodies) over five different devices vs concentrations of S protein in an artificial saliva mixture.

V_{th} over at least eight samples. V_{th} levels of n-antibody-functionalized rGO layers rather have a dependency of BSA incubation time. That is, overnight BSA incubation largely increases V_{th} close to those of bare SiO_2 and APTMS while increasing G_m^{For} loss of the system. This suggested a formation of thick layer of protein in terms of hydrophobic bonding of protein on rGO surfaces covering the most 2D rGO layer areas for this long-term incubation.

We measured eight different rGO devices with 4 h incubation with BSA and n-antibodies (250 μg/mL) in the following S protein tests. Increasing concentrations of S proteins on an n-antibody-functionalized rGO surface induced additional positive surface potentials,[5] with saturation occurring at the concentration of S proteins above 34 ng/mL (Figure 6c, SI Figure S20). ΔV_{th} calculated at a difference in V_{th} at each S protein concentration and baseline V_{th} is used to minimize effects of baseline V_{th} changed by BSA incubations on the calculation of sensitivity. Each ΔV_{th} point in Figure 6c was obtained from the last point of ΔV_{th} for 20 measurements (5 min testing time) at each concentration in SI Figure S21. All ΔV_{th} sensing curves obtained after measurements for at least 2.5 min displayed stable sensing curves in ΔV_{th} but longer measurement time of 5 min was chosen to obtain stable ΔV_{th} levels in quasi-equilibrium, which minimizes the impact of measurement time and drift on the sensitivity of devices (SI Figure S22).

The increased concentration of n-antibodies on the rGO surface from 20 to 250 μg/mL revealed a higher sensitivity and resolution over all ranges of S protein concentrations. For rGO layers functionalized with 250 μg/mL n-antibodies, the sensitivity was measured to be 6.3 mV/dec, with an R^2 of 0.986 at a concentration range of 3.4 pg/mL to 34 ng/mL in a PBS buffer solution. We defined a LOD at the concentration of S proteins showing a clear signal in ΔV_{th} which is distinguishable from the maximum fluctuation in baselines (ca. 10 mV) that could occur for any measurement conditions (SI Figure S22). Thus, the guaranteed LOD is a few pg/mL. After measuring the S protein, the FG surfaces were washed five times with a pure PBS solution and then sequentially measured in a pure PBS again to confirm the remaining binding signals after washing (SI Figure S21). A higher sensitivity was maintained for rGO surfaces functionalized with 250 μg/mL n-antibodies, possibly because of a larger number of binding events between the n-antibody and the S protein, even after washing. After completing all the measurements, we then measured the FG surface for the pH2 buffer solution (SI Figure S21). A sharp shift in the V_{th} in pH2 resulted from $\Delta\varphi_s$ of the rGO layers by pH, indicating the presence of sturdy rGO layers, even after conducting all the sensing experiments.

Opposite ΔV_{th} was observed from a bare rGO layer contacted with the same concentrations of S protein and BSA (Figure 6d, SI Figure S23), supporting the specificity of our results above and strong nonspecific binding of proteins on rGO surfaces in terms of hydrophobic interactions. This result, however, suggests the essential needs for blocking layers for FET bioelectronics to prevent further nonspecific binding. Our

https://doi.org/10.1021/acsami.2c04969
ACS Appl. Mater. Interfaces 2022, 14, 24187−24196

electrical detection signals were verified by the ELISA experiments shown in Figure 6e. We used n-antibody conjugated-rGO substrates processed identically to Figure 6c as a starting surface for ELISA testing by directly placing them on a new well plate to process the rest of ELISA protocol. The n-antibody conjugated-rGO surface with S proteins showed distinguishable signals compared with those with bare rGO surfaces without n-antibody conjugation as the control group. This result explicitly showed *n*-antibodies were successfully functionalized on our rGO surfaces. Moreover, the ELISA signals further increased by 50% by increasing the n-antibody concentration from 20 μg/mL to 250 μg/mL (Figure 6e), which corresponds to our electrical measurements.

Finally, the detection of S proteins was performed in a solution mixture of artificial saliva and 0.05× PBS with a ratio of 1:20 in order to demonstrate the potential of our device platform for practical diagnosis (Figure 6f). Each ΔV_{th} in Figure 6f is an average of five samples. The PBS solution in this mixture plays a role of controlling pH of testing media at pH7.4. This dilution ratio was chosen by finding the minimum dilution ratio of the PBS solution that preserves the pH value of a mixture solution at 7.4 (SI Figure S24). This is especially important for reproducibility of signals because divergent pH of patient's saliva in a range from 6.2 to 7.6 could affect changes in isoelectric point of proteins on sensing surfaces. The sensitivity in saliva-relevant fluids was measured to be 5.1 mV/dec, with an R^2 of 0.984 and CV < 3% (from raw values of V_{th} over five samples), in a range from 500 fg/mL to 5 ug/mL (Figure 6f) while the guaranteed LOD is at pg/mL considering the maximum fluctuation value (ca. 10 mV) in baseline. Our LOD is not as low as other pervious solution-gated 2D FET sensor research[6] although both the RFGFET and conventional solution-gated structures have the same solution interface, that is, between the 2D material and the media solution. For RFGFET, changes in surface potentials are capacitively transferred to the FET transducer as the 2D interface is isolated by the insulator, which suppresses many noise factors but also leads to some loss in specific signals due to the additional process for signal transmission over the insulator. In contrast, for conventional solution-gated structures, all changes in surface potentials on the 2D interface are directly read out by the same 2D semiconductor, which enables higher sensitivity and lower LOD for targeting biomarkers than our RFGFET but allows nonideal signaling to be incorporated into output signals. We emphasize again that the success of COVID-19 FET sensors now depends on how reliable and stable devices are rather than how sensitive they are because reported FET sensors display a sensitivity that is more than enough compared to conventional optical-based analytical tools.[9]

CONCLUSION

To elucidate the critical mechanistic factors behind the instability of rGO layers, we constructed an rGO sensing membrane in the RFGFET setup for rapid and reliable diagnostic tools for detecting COVID-19 as an alternative to current LFAs and RT-PCR methods. We performed a comprehensive systematic analysis of the pH sensing properties of rGO layers affected by their thickness, coverage, and reduction temperature. FG configuration is essential for reducing large device-to-device variations of 2D materials-based bioelectronics. The high conductivity of rGO obtained by high reduction temperatures increased hydrophobicity by reducing oxygen functional groups. A high conductivity achieved by dense networks of rGO plus a minimum reduction temperature leads to the optimal transducing properties, showing a pH sensitivity of 54 mV/pH with an R^2 value of 0.998 and CV < 3%, 90% yield, and a low drift ratio of 2%. As a proof-of-concept, we demonstrated highly reproducible and reliable detection of the COVID-19 S proteins in both 0.05× PBS and a saliva mixture. In response to concentrations of S proteins, our RFGFET sensors displayed the sensitivity of 6.3 mV/dec (3.4 pg/mL to 34 ng/mL) for a 0.05× PBS environment and 5.1 mV/dec (500 fg/mL to 5 μg/mL) with CV < 3% for a saliva mixture solution. The guaranteed LOD of S proteins was at a few pg/mL. The sensitivity and specificity of the SARS-CoV-2 S protein were also confirmed by ELISA. This platform may have an immense effect on positioning FET bioelectronics in a clinical setting for COVID-19 detection.

EXPERIMENTAL SECTION

RG Module Fabrication. The cleaned 4 in silicon wafer with a 300 nm-thick SiO_2 was treated with oxygen plasma for 5 min at 250 W under an O_2 flow rate of 10 sccm in order to introduce hydroxyl groups on SiO_2 surfaces. The wafer was fully immersed and incubated in a 5% APTMS (Sigma-Aldrich, 281778) solution dissolved in ethanol (Sigma-Aldrich, 459836) for 1 h. After washing the surface, the wafer was heated at 120 °C for 20 min. Then, GO solutions of 0.12, 0.24, 0.48, and 0.59 mg/mL were prepared by dispersing GO (ACS Material, 7782−42−5) in deionized water aided by ultrasonication for 20 min. Each GO solution was spin-coated on an APTMS/SiO_2 wafer under 1600 rpm for 1 min. In heat-assisted drop-casting, 16 mL of 0.12 mg/mL solution was drop-casted over the entire area of a 4-in wafer and then baked at 120 °C for 1 h. The GO/APTMS/SiO_2 wafers were sliced to 1 × 2 cm^2 for an RG module. The postannealing of each GO RG module was performed using a horizontal furnace for 5 min under an argon gas environment, with temperatures of 200, 300, and 400 °C. The surface images were acquired by scanning electron microscopy (SEM).

Preparation of *n*-Antibody-Conjugated rGO Layers and Testing Media. The fabricated rGO RG modules were fully immersed in a 10 mg/mL 1-pyrenebutyric acid *N*-hydroxysuccinimide ester, 95% (PBASE) (Santa Cruz Biotechnology, 114932−60−4) solution for 2 h. After washing the rGO surfaces, 20 or 250 μg/mL SARS-CoV-2 neutralizing antibody (Sino Biological, 40592-MM57) was incubated on the rGO surface at least for 4 h. Sequentially, 10 mg/mL BSA solution dissolved in 1× PBS was added at least for 4 h. The SARS-CoV-2 S protein (Sino Biological, 40592-V08B) was diluted in 0.05× PBS to concentrations of 34 fg/mL to 3.4 μg/mL for testing media. Also, S proteins were diluted in a mixture solution of 0.05× PBS and artificial saliva (Fisher Scientific, NC1873811) with a ratio of 20:1 to concentrations of 500 fg/mL to 5 μg/mL for testing media. Initial pH of the artificial saliva was 6.

Electrical Measurement System. A commercial FET (CD4007UB) was used as a transducer to investigate the fabricated RGs, as previously discussed. An aqueous solution at a defined pH was placed on each RG surface. An Ag/AgCl reference electrode was placed in the solution in order to apply the gate bias for all measurements. All transfer curves were measured using a Keithley 4200A semiconductor analyzer with a drain voltage set at 50 mV, and the gate voltage remained in the double-sweep mode. Transfer curves of the RGFET were repeatedly measured for 20 cycles under a pH solution in a range from pH2 to 11. The *Vth* was calculated as the gate voltage corresponding to drain current of 1 μA in each transfer curve. The *Gm* of each RGFET was calculated at its maximum value.

ELISA Protocol. The n-antibody-conjugated rGO substrates sliced to 0.5 × 0.5 cm^2 were placed in a new 48-well plate. Each rGO substrate was washed gently three times with 1× PBS including 0.05% Tween 20. Sequentially, 200 μL of biotinylated spike protein prepared in 1× assay buffer at a concentration of 1 μg/mL (Biolegend) was incubated on each rGO substrate for 2 h under 300 rpm at room

https://doi.org/10.1021/acsami.2c04969
ACS Appl. Mater. Interfaces 2022, 14, 24187−24196

temperature. After gently washing each rGO surface three to five times with 1× PBS including 0.05% Tween 20, 200 μL avidin-HRP (Biolegend) diluted 1000 times in 1× assay buffer was incubated for 30 min with 300 rpm shaking under room temperature, then gently washed five times using 1× PBS including 0.05% Tween 20. The samples were soaked in the buffer for 30 s during each wash. Then, 200 mL 3,3′,5,5′-tetramethylbenzidine substrate was further added into each well and incubated for 30 min under dark. Finally, 200 μL stop reagent (2N H_2SO_4) was added, and the resulting solutions in each well were transferred to another new 48-well plate for measurements. The absorbance values were read at 450 nm using a microplate reader.

■ ASSOCIATED CONTENT

Supporting Information

The Supporting Information is available free of charge at https://pubs.acs.org/doi/10.1021/acsami.2c04969.

Electrical properties of Si-FET transducer. pH responses of transfer curves of RGFET with RGs of SiO_2, APTMS/SiO_2, and rGO/APTMS/SiO_2 which is reduced at different reduction temperatures and coverages. E_{RG}^{For} distributions of bare rGO and n-antibody-functionalized rGO layers for increasing spike proteins. SEM images of rGO layers made by heat-assisted drop-casting method (PDF)

■ AUTHOR INFORMATION

Corresponding Author

Junhong Chen − *Pritzker School of Molecular Engineering, University of Chicago, Chicago, Illinois 60637, United States; Chemical Sciences and Engineering Division, Physical Sciences and Engineering Directorate, Argonne National Laboratory, Lemont, Illinois 60439, United States;* orcid.org/0000-0002-2615-1347; Email: junhongchen@uchicago.edu

Authors

Hyun-June Jang − *Pritzker School of Molecular Engineering, University of Chicago, Chicago, Illinois 60637, United States; Chemical Sciences and Engineering Division, Physical Sciences and Engineering Directorate, Argonne National Laboratory, Lemont, Illinois 60439, United States*

Xiaoyu Sui − *Pritzker School of Molecular Engineering, University of Chicago, Chicago, Illinois 60637, United States; Chemical Sciences and Engineering Division, Physical Sciences and Engineering Directorate, Argonne National Laboratory, Lemont, Illinois 60439, United States*

Wen Zhuang − *Pritzker School of Molecular Engineering, University of Chicago, Chicago, Illinois 60637, United States*

Xiaodan Huang − *Pritzker School of Molecular Engineering, University of Chicago, Chicago, Illinois 60637, United States*

Min Chen − *Pritzker School of Molecular Engineering, University of Chicago, Chicago, Illinois 60637, United States;* orcid.org/0000-0001-7856-8788

Xiaolei Cai − *Pritzker School of Molecular Engineering, University of Chicago, Chicago, Illinois 60637, United States*

Yale Wang − *Department of Mechanical Engineering, University of Wisconsin-Milwaukee, Milwaukee, Wisconsin 53211, United States*

Byunghoon Ryu − *Chemical Sciences and Engineering Division, Physical Sciences and Engineering Directorate, Argonne National Laboratory, Lemont, Illinois 60439, United States;* orcid.org/0000-0003-3654-6198

Haihui Pu − *Pritzker School of Molecular Engineering, University of Chicago, Chicago, Illinois 60637, United States; Chemical Sciences and Engineering Division, Physical Sciences and Engineering Directorate, Argonne National Laboratory, Lemont, Illinois 60439, United States*

Nicholas Ankenbruck − *Pritzker School of Molecular Engineering, University of Chicago, Chicago, Illinois 60637, United States*

Kathleen Beavis − *Department of Pathology, University of Chicago, Chicago, Illinois 60637, United States*

Jun Huang − *Pritzker School of Molecular Engineering, University of Chicago, Chicago, Illinois 60637, United States;* orcid.org/0000-0003-0271-4384

Complete contact information is available at: https://pubs.acs.org/10.1021/acsami.2c04969

Author Contributions

Electrical Measurement, sample Fabrication, interpretation of data were carried out by H.-J.J., X.S., W.Z., Y.W., and B.R. ELISA measurement and analysis were performed by X.H., M.C., and J.H. The manuscript was prepared by H.-J.J., H.P., N.A., and J.C. All authors examined and commented on the manuscript. The project was guided by J.C., K.B., and J.H.

Notes

The authors declare no competing financial interest.

■ ACKNOWLEDGMENTS

This work was supported by a Walder Foundation grant and a University of Chicago Big Ideas Generator grant.

■ REFERENCES

(1) Yuki, K.; Fujiogi, M.; Koutsogiannaki, S. COVID-19 Pathophysiology: A Review. *Clin. Immunol.* **2020**, *215*, 108427.

(2) Peck, K. R. Early Diagnosis and Rapid Isolation: Response to COVID-19 Outbreak in Korea. *Clin. Microbiol. Infec.* **2020**, *26*, 805−807.

(3) Afzal, A. Molecular Diagnostic Technologies for COVID-19: Limitations and Challenges. *J. Adv. Res.* **2020**, *26*, 149−159.

(4) Perchetti, G. A.; Huang, M. L.; Mills, M. G.; Jerome, K. R.; Greninger, A. L. Analytical Sensitivity of the Abbott BinaxNOW COVID-19 Ag Card. *J. Clin. Microbiol.* **2021**, *59*, e02880−20.

(5) Zamzami, M. A.; Rabbani, G.; Ahmad, A.; Basalah, A. A.; Al-Sabban, W. H.; Ahn, S. N.; Choudhry, H. Carbon Nanotube Field-Effect Transistor (CNT-FET)-based Biosensor for Rapid Detection of SARS-CoV-2 (COVID-19) Surface Spike Protein S1. *Bioelectrochemistry* **2022**, *143*, 107982.

(6) Seo, G.; Lee, G.; Kim, M. J.; Baek, S. H.; Choi, M.; Ku, K. B.; Lee, C. S.; Jun, S.; Park, D.; Kim, H. G.; Kim, S. J.; Lee, J. O.; Kim, B. T.; Park, E. C.; Kim, S. I. Rapid Detection of COVID-19 Causative Virus (SARS-CoV-2) in Human Nasopharyngeal Swab Specimens Using Field-Effect Transistor-Based Biosensor (vol 14, pg 5135, 2020). *ACS Nano* **2020**, *14*, 12257−12258.

(7) Li, J.; Wu, D.; Yu, Y.; Li, T.; Li, K.; Xiao, M. M.; Li, Y.; Zhang, Z. Y.; Zhang, G. J. Rapid and Unamplified Identification of COVID-19 with Morpholino-modified Graphene Field-Effect Transistor Nanosensor. *Biosens. Bioelectron.* **2021**, *183*, 113206.

(8) Fathi-Hafshejani, P.; Azam, N.; Wang, L.; Kuroda, M. A.; Hamilton, M. C.; Hasim, S.; Mahjouri-Samani, M. Two-Dimensional-Material-Based Field-Effect Transistor Biosensor for Detecting COVID-19 Virus (SARS-CoV-2). *ACS Nano* **2021**, *15*, 11461−11469.

(9) Baker, A.; Richards, S. J.; Congdon, T.; Hasan, M.; Guy, C.; Zwetsloot, A.; Gallo, A.; Lewandowski, J.; Stansfeld, P.; Straube, A.; Walker, M.; Chessa, S.; Pergolizzi, G.; Dedola, S.; Field, R.; Gibson, M. The SARS-COV-2 Spike Protein Binds Sialic Acids, and Enables Rapid Detection in a Lateral Flow Point of Care Diagnostic Device. *ACS Central. Sci.* **2021**, *7* (2), 379−380.

(10) Kutovyi, Y.; Hlukhova, H.; Boichuk, N.; Menger, M.; Offenhausser, A.; Vitusevich, S. Amyloid-beta Peptide Detection via Aptamer-Functionalized Nanowire Sensors Exploiting Single-Trap Phenomena. *Biosens. Bioelectron.* **2020**, *154*, 112053.
(11) Alabsi, S. S.; Ahmed, A. Y.; Dennis, J. O.; Khir, M. H. M.; Algamili, A. S. A Review of Carbon Nanotubes Field Effect-Based Biosensors. *IEEE Access* **2020**, *8*, 69509−69521.
(12) Sarkar, D.; Liu, W.; Xie, X. J.; Anselmo, A. C.; Mitragotri, S.; Banerjee, K. MoS2 Field-Effect Transistor for Next-Generation Label-Free Biosensors. *ACS Nano* **2014**, *8*, 3992−4003.
(13) Tsang, D. K. H.; Lieberthal, T. J.; Watts, C.; Dunlop, I. E.; Ramadan, S.; Hernandez, A. E. D.; Klein, N. Chemically Functionalised Graphene FET Biosensor for the Label-free Sensing of Exosomes. *Sci. Rep.* **2019**, *9*, 13946.
(14) Hwang, M. T.; Heiranian, M.; Kim, Y.; You, S.; Leem, J.; Taqieddin, A.; Faramarzi, V.; Jing, Y. H.; Park, I.; van der Zande, A. M.; Nam, S.; Aluru, N. R.; Bashir, R. Ultrasensitive Detection of Nucleic Ccids Using Deformed Graphene Channel Field Effect Biosensors. *Nat. Commun.* **2020**, *11*, 1543.
(15) Park, D.; Kim, J. H.; Kim, H. J.; Lee, D.; Lee, D. S.; Yoon, D. S.; Hwang, K. S. Multiplexed Femtomolar Detection of Alzheimer's Disease Biomarkers in Biofluids Using a Reduced Graphene Oxide Field-Effect Transistor. *Biosens. Bioelectron.* **2020**, *167*, 112505.
(16) Fan, Q.; Wang, L. D.; Xu, D.; Duo, Y. H.; Gao, J.; Zhang, L.; Wang, X. B.; Chen, X.; Li, J. H.; Zhang, H. Solution-Gated Transistors of Two-Dimensional Materials for Chemical and Biological Sensors: Status and Challenges. *Nanoscale* **2020**, *12* (21), 11364−11394.
(17) Fu, W. Y.; Nef, C.; Knopfrnacher, O.; Tarasov, A.; Weiss, M.; Calame, M.; Schonenberger, C. Graphene Transistors Are Insensitive to pH Changes in Solution. *Nano Lett.* **2011**, *11*, 3597−3600.
(18) Ang, P. K.; Chen, W.; Wee, A. T. S.; Loh, K. P. Solution-Gated Epitaxial Graphene as pH Sensor. *J. Am. Chem. Soc.* **2008**, *130*, 14392−14393.
(19) Yu, Q. K.; Lian, J.; Siriponglert, S.; Li, H.; Chen, Y. P.; Pei, S. S. Graphene Segregated on Ni surfaces and Transferred to Insulators. *Appl. Phys. Lett.* **2008**, *93*, 113103.
(20) Kim, K. S.; Zhao, Y.; Jang, H.; Lee, S. Y.; Kim, J. M.; Kim, K. S.; Ahn, J. H.; Kim, P.; Choi, J. Y.; Hong, B. H. Large-scale Pattern Growth of Graphene Films for Stretchable Transparent Electrodes. *Nature* **2009**, *457*, 706−710.
(21) Yan, F.; Zhang, M.; Li, J. H. Solution-Gated Graphene Transistors for Chemical and Biological Sensors. *Adv. Healthc. Mater.* **2014**, *3*, 313−331.
(22) Howarter, J. A.; Youngblood, J. P. Surface Modification of Polymers with 3-aminopropyltriethoxysilane as a General Pretreatment for Controlled Wettability. *Macromolecules* **2007**, *40*, 1128−1132.
(23) Ke, Z. L.; Oton, J. Q.; Qu, K.; Cortese, M.; Zila, V.; McKeane, L.; Nakane, T.; Zivanov, J.; Neufeldt, C. J.; Cerikan, B.; Lu, J. M.; Peukes, J.; Xiong, X. L.; Krausslich, H. G.; Scheres, S. H. W.; Bartenschlager, R.; Briggs, J. A. G. Structures and Distributions of SARS-CoV-2 Spike Proteins on Intact Virions. *Nature* **2020**, *588*, 498−502.
(24) Li, Y. R.; Chang, S. H.; Chang, C. T.; Tsai, W. L.; Chiu, Y. K.; Yang, P. Y.; Cheng, H. C. High-sensitivity Extended-Gate Field-Effect Transistors as pH sensors with Oxygen-Modified Reduced Graphene Oxide Films Coated on Different Reverse-Pyramid Silicon Structures as Sensing Heads. *Jpn. J. Appl. Phys.* **2016**, *55*, 04em08.
(25) Li, L.; Ma, X. F.; Xiao, Y.; Wang, Y. Construction and Application of Graphene Oxide-Bovine Serum Albumin Modified Extended Gate Field Effect Transistor Chiral Sensor. *Sensors* **2021**, *21*, 3921.
(26) Jang, H. J.; Wagner, J.; Li, H.; Zhang, Q. Y.; Mukhopadhyaya, T.; Katz, H. E. Analytical Platform To Characterize Dopant Solution Concentrations, Charge Carrier Densities in Films and Interfaces, and Physical Diffusion in Polymers Utilizing Remote Field-Effect Transistors. *J. Am. Chem. Soc.* **2019**, *141*, 4861−4869.
(27) Pullano, S. A.; Critello, C. D.; Mahbub, I.; Tasneem, N. T.; Shamsir, S.; Islam, S. K.; Greco, M.; Fiorillo, A. S. EGFET-Based Sensors for Bioanalytical Applications: A Review. *Sensors* **2018**, *18*, 4042.
(28) Jang, H. J.; Song, Y. J.; Wagner, J.; Katz, H. E. Suppression of Ionic Doping by Molecular Dopants in Conjugated Polymers for Improving Specificity and Sensitivity in Biosensing Applications. *ACS Appl. Mater. Interfaces* **2020**, *12*, 45036−45044.
(29) Jang, H. J.; Wagner, J.; Song, Y. J.; Lee, T.; Katz, H. E. Carboxylic Acid-Functionalized Conjugated Polymer Promoting Diminished Electronic Drift and Amplified Proton Sensitivity of Remote Gates Compared to Nonpolar Surfaces in Aqueous Media. *Adv. Electron. Mater.* **2020**, *6*, 1901073.

https://doi.org/10.1021/acsami.2c04969
ACS Appl. Mater. Interfaces 2022, 14, 24187−24196